Macromolecular Materials and Engineering
Open Access
www.mame-journal.de

Tailoring the Multifunctional Properties of PA6/PA12 75/25 Conductive Polymer Composites With Carbon Nanotubes

*T. Arnal, P. Eisenberg, A. Ares-Pernas, C. Bernal, and M. J. Abad**

Conductive polymer composites (CPCs) offer a unique combination of the lightweight and processable nature of polymers with the electrical conductivity of metals, making them suitable for a range of applications, including electromagnetic interference shielding and sensors. This study investigates the multifunctional properties of polyamide 6/polyamide 12 (PA6/PA12) (75/25) CPCs filled with multi-walled carbon nanotubes (MWCNTs). The present research focuses on the morphological, rheological, thermal, and electrical properties of nanocomposites. The incorporation of MWCNTs into the PA6/PA12 blend is achieved using twin-screw extrusion, and compression molding is used to obtain nanocomposites. Different MWCNT loadings are examined to optimize the dispersion and connectivity of the conductive filler network. Morphological analysis via scanning electron microscopy reveals significant structural changes with increasing MWCNT content, changing from a sea-island morphology to a more interconnected network. Differential scanning calorimetry provides insights into the thermal behavior, showing changes in melting and crystallization behavior as well as crystallinity degree with filler loading. Rheological assessments demonstrated variations in complex viscosity, storage modulus, and loss modulus with different MWCNT contents. Electrical measurements using the Van der Pauw technique highlightes the improved conductivity of the nanocomposites. The findings underscore the potential of PA6/PA12/MWCNT nanocomposites for advanced applications such as interference shielding and sensors.

1. Introduction

CPCs have emerged as a class of materials that bridge the gap between the lightweight processability of polymers and the electrical conductivity of metals. Typically, polymers act as insulators, however when they are mixed with conductive fillers such as carbon nanotubes (CNTs) or metal particles, they become multifunctional composites. These versatile materials offer potential for various applications including electromagnetic interference (EMI) shielding[1–4] sensors,[5–7] and energy storage devices,[8–11] among others.

Developing CPCs involves the challenge of achieving a network of conductive fillers. This means ensuring a uniform distribution of the particles throughout the polymer matrix to maximize their connectivity and minimize the required filler amount for efficient electrical conduction (percolation threshold). Many research groups initially focused on strategies involving a single polymer but encountered difficulties in achieving optimal filler distribution. As a result, they shifted towards exploring polymer blends, observing improved control over filler localization by combining two or more immiscible polymers with distinct properties. The preferred localization of fillers at the interface between these polymers led to a more defined segregated network

T. Arnal, C. Bernal
Universidad de Buenos Aires
Facultad de Ingeniería
Av. Paseo Colón 850, Buenos Aires C1063, Argentina

T. Arnal, C. Bernal
CONICET – Universidad de Buenos Aires
Instituto de Tecnología en Polímeros y Nanotecnología (ITPN)
Av. Gral. Las Heras 2214, Buenos Aires C1119, Argentina

P. Eisenberg
Instituto de Investigación e Ingeniería Ambiental -3iA, EHyS
Universidad Nacional de San Martín
25 de Mayo y Francia, San Martín, Buenos Aires 1650, Argentina

A. Ares-Pernas, M. J. Abad
Universidade da Coruña
Campus Industrial de Ferrol
CITENI-Grupo de Polímeros, Campus de Esteiro, A Coruña, Ferrol 15403, Spain
E-mail: maria.jose.abad@udc.es

The ORCID identification number(s) for the author(s) of this article can be found under https://doi.org/10.1002/mame.202400443

DOI: 10.1002/mame.202400443

and enhanced electrical properties.[12] Recent research has further refined this approach by investigating the use of polymer blends from the same family, such as polyamides,[13–16] showing promising results.

The knowledge of the rheological properties of CPCs is crucial for optimizing their processing.[17,18] Rheology refers to the flow behavior of materials under stress. By studying these properties, the processing techniques, such as extrusion or injection molding, can be tailored to achieve the desired microstructure and ultimately, the targeted electrical performance.

The focus of research then shifts to the electrical properties of the optimized CPCs. By carefully designing the composite structure, researchers can achieve electrical conductivity suitable for diverse applications.[19,20] This includes fabricating highly sensitive sensors for detecting pressure, temperature, or chemical changes. Additionally, precisely controlled conductivity allows for effective EMI shielding, protecting electronic devices from electromagnetic interference.

This work aims to go deeper into the recent advancements in engineering CPCs, exploring strategies for achieving improved conductive networks, optimizing rheological, morphological, and thermal properties for efficient processing, and ultimately, tailoring the electrical properties for targeted applications in sensors and EMI shielding, among others. Significant structural variations with increasing filler content were observed, changing from a sea-island morphology in the neat blend to more interconnected networks of MWCNTs in the nanocomposites, exhibiting improved electrical properties. In addition, variations in melting and crystallization behavior as well as in storage modulus and loss modulus with filler loading were found.

2. Experimental Section

2.1. Materials

Polyamide 12 (PA12 Grilamid supplied by EMS Grivory, T_m = 180 °C, δ = 1.01 g cm^{-3} MFI = 50 cm^3/10 min, and Polyamide 6 (PA6 Zytel supplied by DuPont, T_m = 220 °C δ = 1.14 g/cm^3, MFI = 24.02 cm^3/10 min) were used. To prepare the nanocomposites, a commercial masterbatch of multi-walled carbon nanotubes (MWCNTs) (PLASTICYL PA1503, Nanocyl S.A, Sambreville, Belgium) pre-dispersed at 15 wt.% in PA6 was employed. The PA6 used in the masterbatch was the same grade as that of the pure PA6. According to the supplier, the MWCNTs have an average diameter of 9.5 10^{-9} m, an average length of 1.5 µm, a carbon purity of 90%, a surface area of 250–300 m^2 g^{-1}, and a volume resistivity of 10^{-4} Ωcm.

2.2. Preparation of Nanocomposites

Different contents of MWCNTs (ranging from 0 to 11 wt. %) were incorporated into a 75/25 wt.% PA6/PA12 blend and processed using a co-rotating twin-screw extruder (Brabender DSE 20) at a speed of 20 rpm and a temperature range of 225–240 °C. All materials were premixed by tumbling before being simultaneously fed into the extruder. Prior to this, the masterbatch and the pure polyamides underwent drying in an oven at 80 °C for 18 hours.

Table 1. Nomenclature of the different nanocomposites based on PA6, PA12 and MWCNTs.

Base material			MWCNT content (wt.%)	Nomenclature
PA6 (%)	PA12 (%)	PA6/MWCNTs masterbatch (%)		
75	25	0	0	7525–0
73.40	24.93	1.66	0.25	7525–0.25
71.79	24.88	3.33	0.5	7525–0.5
68.58	24.75	6.67	1	7525–1
65.37	24.63	10.00	1.5	7525–1.5
62.17	24.50	13.33	2	7525–2
58.95	24.38	16.67	2.5	7525–2.5
52.54	24.13	23.33	3.5	7525–3.5
42.92	23.75	33.33	5	7525–5
23.67	23.00	53.33	8	7525–8
4.42	22.25	73.33	11	7525–11

The different pellets obtained by extrusion (dried in an oven at 80 °C for 18 h) were subjected to compression molding in a hot-plate press (IQAP-LAP, model PL-15) at a temperature of 245 °C under a pressure of 15 MPa for 2 minutes. Circular samples with a diameter of 25 mm and a nominal thickness of 3 mm were produced. The different samples, along with their specific names, were detailed in **Table 1**.

2.3. Morphological Evaluation by Scanning Electron Microscopy

Scanning electron microscopy (SEM) was used to evaluate the surface morphology of samples cryo-fractured at liquid nitrogen temperature and then coated with a thin layer of gold. SEM micrographs were obtained using a field emission scanning electron microscope (JEOL FSEM JS4-7200F) at an accelerating voltage of 5 kV.

2.4. Thermal Analysis

Thermal analysis was performed using a differential scanning calorimeter (DSC-2010, TA Instruments). Samples were first heated under nitrogen atmosphere at a rate of 10 °C min^{-1} from 0 °C to 250 °C, held isothermally for 5 min to erase thermal history, and then cooled back to 0 °C at the same rate. A second heating cycle with identical parameters was performed. The DSC curves from the cooling and second heating scans were analyzed to determine melting temperature (T_m), crystallization temperature (T_c) and crystallinity degree (X_c) of the samples.

Thermal parameters were obtained using the Universal Analysis 2000 software (Ver. 4.5A, TA Instruments). The crystallinity degree was calculated following Equation (1), where ΔH^*_m was the melting enthalpy normalized to the polyamide fraction.

$$X_c\ (\%) = \frac{\Delta H^*_m}{\Delta H_0} \quad (1)$$

The heat of fusion of 100% crystalline polyamides was taken as ΔH_0 = 230 J g^{-1} for PA6[21] and ΔH_0 = 209 J g^{-1} for PA12.[22]

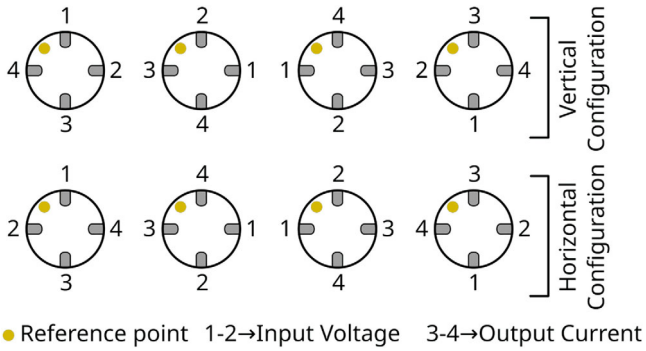

Figure 1. Scheme of the electrical measurement setup used to determine the conductivity of the different samples.

2.5. Rheological Assessment

Rheological tests were conducted at 230 °C using a controlled strain rheometer (ARES, TA Instruments) equipped with parallel plate geometry (25 mm diameter, 1 mm gap). The measurements included the determination of complex viscosity (η^*), storage modulus (G'), and loss modulus (G'') varying frequencies (ω). The rheological experiments were carried out within the linear viscoelastic region, which had been established through a preliminary strain sweep test. Frequency sweep measurements were conducted within a range of 0.1 to 100 rad/s.

2.6. Electrical Measurements

To determine the electrical conductivity of the different nanocomposites obtained, the resistance of the samples was measured using a SMU device (2450 Keithley Instruments) employing the Van der Pauw technique. This method for measuring resistivity utilizes a constant-current method, making it particularly advantageous for evaluating very small samples. This technique was unaffected by the dimensions of the sample or the spacing of the contacts. It employs four isolated contacts arranged on the periphery of a flat, arbitrarily shaped sample. Eight measurements per sample were performed around the sample to determine the sheet resistance, where a voltage sweep between −40 to 40 V was introduced in 1–2 (input) and the current was measured in 3–4 (output) (**Figure 1**), which was then used to calculate the conductivity of the material,[23] according to Equation (2),

$$f(\sigma) = e^{-\pi \cdot R_v \cdot t \cdot \sigma} + e^{-\pi \cdot R_h \cdot t \cdot \sigma} - 1 \quad (2)$$

where R_v was the mean value of the resistance in the vertical configuration, R_h was the mean value of the resistance in the horizontal configuration, t was the thickness of the sample and σ the volumetric conductivity of the material.

In this work, samples surfaces were polished using a fine sandpaper and four points were two times coated with silver paint (Figure 1) to ensure good contact between the material and the connectors.

3. Results and Discussion

3.1. Morphological Analysis

Figure 2 illustrates the morphology of the PA6/PA12 75/25 blend and the nanocomposites containing varying amounts of MWCNTs. The neat polyamide blend (Figure 2a) displays a characteristic sea-island morphology composed of PA12 nearly spherical second-phase particles rather homogeneously distributed within a PA6 matrix. This is indicative of a phase-separated structure which is a common feature observed in immiscible polymer blends. This micro-scale phase separation arises due to the inherent immiscibility between the different polymer components that depends on interfacial tension, viscosity ratio, volume fraction and processing conditions,[24,25] leading to the formation of discrete domains with distinct morphological characteristics.

For the blends with low filler contents (Figure 2b), the sea-island morphology remains evident, but the addition of MWCNTs begins to impact the material´s microstructure. As the nanotubes are incorporated, the dispersed phase particles become smaller primarily due to the MWCNTs acting as compatibilizing agents that could tailor the interfacial tension between PA6 and PA12 phases.[26] Additionally, the surface pattern becomes thinner and denser in corresponding samples. Furthermore, localized regions of high concentration of relatively well-dispersed carbon nanotubes are also evident in the highest magnification SEM micrographs of those samples (insert of Figure 2b). This selective distribution of MWCNTs is attributed to their preferential interaction with PA6, driven by stronger polar interactions with its amide groups compared to PA12. In contrast, PA12, due to its extended hydrocarbon chain segments between amide groups, exhibits a weakly polarized structure resulting in reduced interactions with the MWCNT surface.[27,28] However, MWCNT dispersion and distribution has a minor disruptive effect on the matrix blend's sea-island morphology which still prevails for the low filler loading range investigated.

As the MWCNT content further increases within the intermediate filler content range (Figure 2c–e), a clear transition in the overall morphological characteristics can be observed. In Figure 2c for the sample with 2.5 wt.% MWCNT, while some isolated islands of the dispersed phase are still visible, they are increasingly interspersed with growing interconnected networks of MWCNT-rich regions. This network formation could be driven by the increasing nanotube-nanotube interactions and their tendency to form conductive pathways through the MWCNT-rich zones.[29] Further increasing the MWCNT content (Figure 2d and e for 3.5 and 5 wt.%, respectively), the presence of larger MWCNT-rich zones disrupts the matrix blend´s morphology more significantly, leading to a more interconnected structure. The sea-island morphology becomes less apparent, and the MWCNT-rich zone network begins to dominate the microstructure.[30]

For the highest MWCNT content assayed (11 wt.%, Figure 2f) a drastically altered morphology is observed, where the original sea-island structure is no longer distinguishable and is replaced by a dense network of MWCNT-rich zones. At this concentration, the extensive nanotube network creates a percolated structure throughout the highest affinity PA6 phase, while also probably forcing some nanotubes into the PA12 domains due to space con-

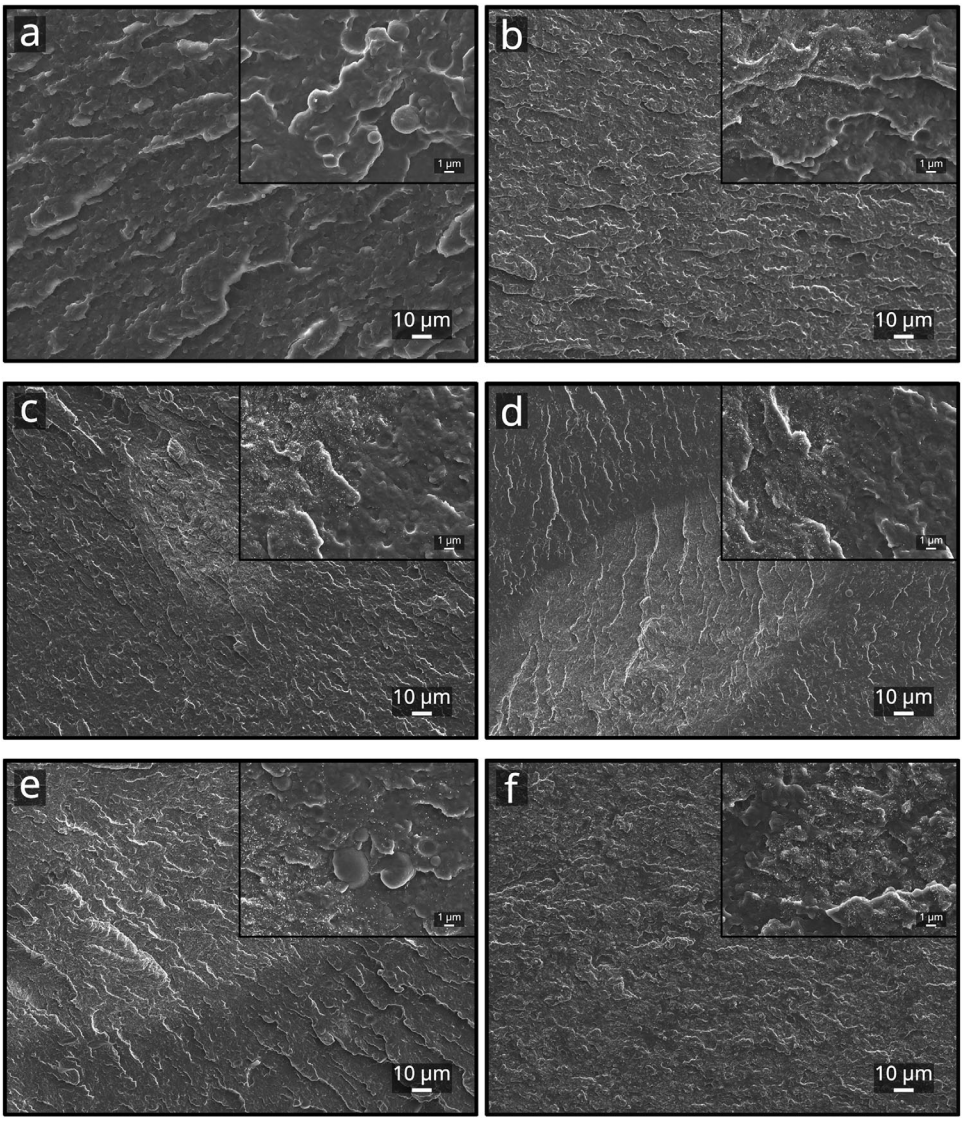

Figure 2. SEM micrographs of cryo-fractured samples of the PA6/PA12 75/25 blend and the nanocomposites with different contents of MWCNTs. a) 7525–0, b) 7525–0.25, c) 7525–2.5, d) 7525–3.5, e) 7525–5 and f) 7525–11. (Closer views can be observed in the inserts on the top right corner of each image).

straints. The surface pattern becomes even thinner and denser exhibiting a highly interconnected nanotube-rich zone network and thus, disrupting the previous microstructural features.

All the distinct features observed in the SEM images have been highlighted and they are available in the supporting information.

3.2. Thermal Behavior

Figure 3 shows the cooling and second heating DSC thermograms of the PA6/PA12 75/25 blend and the nanocomposites with varying content of MWCNTs, and **Tables 2** and **3** list thermal parameters values obtained from the cooling and second heating scans, respectively.

The cooling scans of the nanocomposites (Figure 3a) revealed a slight increase in the crystallization temperatures compared to neat polyamides. The change occurs mainly in PA6, where the peak and onset temperatures increase with the concentration of nanotubes. This suggests that the MWCNTs acted as nucleating agents mainly in the PA6 matrix. This thermal behavior is consistent with the greater chemical affinity of MWCNTs with PA6 compared to the other polyamide (less polar). According to the literature,[27,31] carbon nanotubes had minimal impact on PA12, particularly when compared to the substantial changes observed in PA6's melting characteristics. Similarly, in the present work, this pattern was also reflected in crystallinity measurements, where PA12 showed no significant modifications. Conversely, the crystallization behavior of PA6 was significantly affected. From the incorporation of 2 wt.% MWCNTs, a shoulder peak began to appear for PA6 crystallization. At 3.5 wt.% MWCNT loading, a more well-defined second crystallization peak emerged (around 207 °C). As the MWCNT content increased further, the intensity

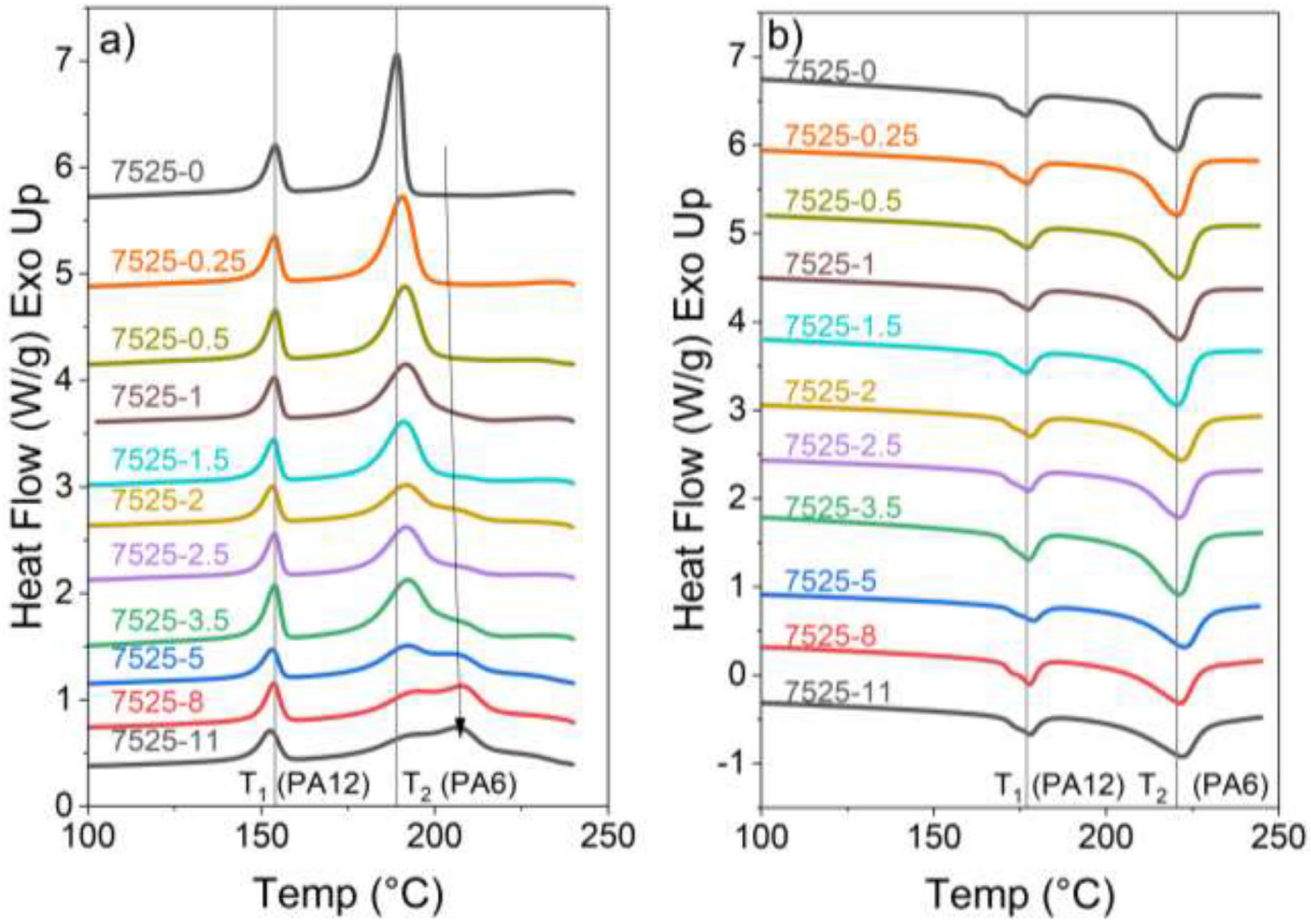

Figure 3. a) Cooling and b) second heating thermograms of the PA6/PA12 75/25 blend and the nanocomposites with different contents of MWCNTs.

of this second peak also increased, eventually surpassing the intensity of the first peak.

Consistent with the results obtained in a previous work on nanocomposites based on a PA6/PA12 50/50 blend,[16] two crystallization peaks for PA6 were observed at 207 °C and 190 °C (Table 2). In the present work, in the PA6/PA12 75/25 nanocomposites with 2, 2.5, and 3.5 wt.% MWCNT, the intensity of the first peak (Tc = 207 °C) was significantly lower compared to the PA6/PA12 50/50 nanocomposites, where the first peak was well separated from the second at 2.5 wt.% MWCNT. For the PA6/PA12 75/25 nanocomposite with 5 wt.% MWCNT, the first peak remained less intense than the second (peak height ratio at 207 °C/190 °C < 1). However, at 8 wt.% MWCNT, an inversion in the peak height ratio occurred, similar to the behavior observed in the nanocomposites based on the PA6/PA12 50/50 blend. This ratio was maintained for the nanocomposite with 11 wt.% MWCNT. The presence of a second crystallization peak can be attributed to two factors: the formation of different crystal morphologies or a two-step crystallization process (as it was previously discussed by Arboleda et al.[14] and Arnal et al.[16]). This behavior is likely to be influenced by both the PA12/PA6 ratio and the MWCNT content.

The choice of the polyamide used in the MWCNT masterbatch was found to slightly influence the crystallization behavior of the polyamides, being this effect more pronounced in PA6. This observation is based on the previous results reported by Arnal et al.[16] for PA6/PA12 50/50 nanocomposites containing MWCNTs dispersed in a PA12/MWCNTs masterbatch and on the results of this work for the PA6/PA12 75/25

Table 2. Crystallization temperatures of the PA6/PA12 75/25 blend and the nanocomposites with different contents of MWCNTs obtained from the cooling thermograms.

Sample	Crystallization Onset [°C]		Crystallization peak [°C]		
	T_1 (PA12)	T_2 (PA6)	T_1 (PA12)	T_2 (PA6)	
7525–0	157.0 (0.2)	192.0 (0.1)	153.8 (0.2)	188.9 (0.2)	–
7525–0.25	156.6 (0.3)	196.5 (0.2)	153.5 (0.3)	190.6 (0.1)	–
7525–0.5	156.7 (0.4)	198.6 (0.3)	153.7 (0.5)	191.1 (0.5)	–
7525–1	156.5 (0.1)	200.7 (0.5)	153.7 (0.1)	191.6 (0.1)	–
7525–1.5	156.4 (0.1)	199.5 (0.1)	153.6 (0.1)	191.3 (0.2)	–
7525–2	156.1 (0.4)	204.5 (2.2)	152.9 (0.3)	191.8 (0.1)	–
7525–2.5	156.8 (0.3)	201.2 (0.1)	154.0 (0.4)	192.1 (0.3)	–
7525–3.5	156.7 (0.3)	217.3 (1.0)	153.9 (0.4)	192.4 (0.9)	207.1 (0.5)
7525–5	156.4 (0.2)	216.4 (0.7)	153.3 (0.3)	192.2 (0.1)	206.3 (0.8)
7525–8	156.7 (0.5)	217.3 (0.6)	153.5 (0.1)	195.0 (0.7)	207.4 (0.3)
7525–11	157.4 (0.5)	217.2 (0.4)	152.9 (0.4)	196.1 (0.1)	206.6 (0.1)

Table 3. Melting and crystallinity parameters of the PA6/PA12 75/25 blend and the nanocomposites with different contents of MWCNTs obtained from the second heating thermograms.

Sample	Melting Onset [°C]		Melting peak [°C]		Enthalpy [J g^{-1}]		Crystallinity X_c [%]	
	T_1 (PA12)	T_2 (PA6)	T_1 (PA12)	T_2 (PA6)	ΔH_m T_1 (PA12)	ΔH_m T_2 (PA6)	PA12	PA6
7525–0	168.2 (0.1)	208.7 (0.1)	176.7 (0.1)	220.4 (0.1)	47.2 (1.3)	58.7 (0.9)	22.6 (0.6)	25.5 (0.4)
7525–0.25	168.3 (0.1)	208.6 (0.2)	177.0 (0.1)	220.6 (0.1)	46.3 (3.2)	54.9 (1.5)	22.1 (1.5)	23.9 (0.7)
7525–0.5	168.0 (0.2)	208.2 (0.1)	177.0 (0.3)	220.7 (0.5)	49.3 (4.1)	58.7 (1.5)	23.6 (2.0)	25.5 (0.6)
7525–1	168.2 (0.5)	207.2 (0.2)	177.1 (0.4)	220.8 (0.4)	42.6 (0.4)	60.1 (0.9)	20.4 (0.2)	26.1 (0.4)
7525–1.5	168.4 (0.2)	207.9 (0.2)	177.1 (0.2)	220.9 (0.2)	45.0 (1.4)	57.5 (2.2)	21.5 (0.7)	25.0 (1.0)
7525–2	169.2 (0.1)	207.0 (0.8)	178.3 (0.1)	221.9 (0.1)	42.3 (1.6)	51.8 (6.0)	20.2 (0.8)	22.5 (2.5)
7525–2.5	168.8 (0.1)	207.4 (0.1)	177.4 (0.1)	220.9 (0.3)	45.9 (4.1)	58.0 (5.0)	22.0 (1.9)	25.2 (2.2)
7525–3.5	169.5 (0.5)	206.5 (1.3)	178.2 (0.7)	221.8 (0.8)	36.1 (4.6)	64.5 (8.3)	17.3 (2.2)	28.1 (3.6)
7525–5	169.7 (0.5)	206.2 (0.4)	178.6 (0.3)	222.2 (0.4)	41.2 (8.0)	63.6 (2.4)	19.7 (3.8)	27.7 (1.0)
7525–8	169.4 (0.4)	204.2 (0.2)	178.0 (0.3)	221.7 (0.4)	49.9 (10.1)	67.0 (5.5)	23.9 (4.9)	29.1 (2.4)
7525–11	170.0 (0.4)	203.9 (0.4)	178.2 (0.2)	222.2 (0.1)	39.5 (3.5)	61.7 (2.2)	18.9 (1.7)	26.8 (0.9)

nanocomposites with MWCNTs dispersed in a PA6/MWCNTs masterbatch.

On the other side, a single endothermic melting peak was observed for each polyamide in the 7525-0 blend (176.7 °C for PA12 and 220.4 °C for PA6) (Figure 3b, Table 3). While the incorporation of carbon nanotubes did not significantly alter the main melting peaks of both PAs (only a slight increase in the melting temperature from the addition of MWCNT contents above 3.5 wt.% was observed), PA6 exhibited a decreasing trend in its onset melting temperature with increasing MWCNT content. This trend is accompanied by a subsequent broadening of the endothermic peak, suggesting the formation of a more heterogeneous crystallite size distribution with varying melting temperatures.[32]

The 7525-0 blend and the nanocomposites with low contents of MWCNTs exhibited a small difference in crystallinity between the two polyamides. These results can be explained by the sequential crystallization mechanism: given that the crystallization temperature (Tc) of PA6 (Figure 3a) is higher than that of PA12, PA6 crystals inevitably form first during the cooling process, preceding PA12 crystallization. This chronological sequence results in PA6 crystallites impeding the subsequent crystallization of PA12 chains. At MWCNT contents higher than 3.5 wt.% the difference between PA6 and PA12 crystallinity values was found to increase and remain roughly constant with filler loading. The observed phenomenon can be attributed to the development of interconnected MWCNT-rich network structures throughout the polymer matrix, as previously detailed in the morphological analysis section, which presumably imposed additional constraints on the formation of ordered crystalline domains. This could be attributed to the limited space and confinement effect (steric hindrance effect) imposed on the polymer chains by the MWCNTs, irrespective of the heterogeneous nucleation effect induced by these fillers.[33–35]

SEM observations corroborate DSC findings, indicating that the presence of MWCNTs affects the melting and crystallization behavior. The uniform distribution of MWCNTs-rich zones at lower concentrations promoted crystals nucleation, particularly for PA6. Conversely, at higher filler concentrations, the limited space and confinement effects imposed on the polymer chains by the MWCNTs may have contributed to decreased crystallinity for the blends containing 11 wt.% of MWCNT, regardless of the heterogeneous nucleation effect induced by these fillers.

3.3. Rheological Behavior

Viscoelastic properties of the nanocomposites as a function of the carbon nanotube loading are shown in **Figure 4**. Even at low filler concentrations the effect over the rheological properties was evident. The complex viscosity (η^*) of the neat blend and nanocomposites, depicted in Figure 4a, was found to decrease as the angular frequency (ω) increased. Moreover, this effect became more pronounced with increasing filler loading, resulting in a shear thinning behavior.[36,37] The increase of η^* at low frequencies confirmed that MWCNTs acted as reinforcing fillers, hindering the flow of polymer chains. The results shown in Figure 4b and c indicate that the storage modulus (G') and loss modulus (G'') both increased as the angular frequency and MWCNT content were raised. The increase in storage modulus with MWCNT content can be explained by the reinforcing effect of the MWCNTs. These nanotubes acted as stiff fillers, impeding the movement of polymer chains and ultimately resulting in a more elastic material. Similarly, the rise in storage modulus with angular frequency is associated with reduced relaxation time for polymer chains at higher frequencies, leading to a more elastic response. The increase in loss modulus with MWCNT content can be attributed to the formation of a network structure by the MWCNTs, which hindered the flow of polymer chains and led to increased viscosity. Additionally, the increase in loss modulus with angular frequency may be due to longer relaxation times for polymer chains at lower frequencies, resulting in a more viscous response.[26,38,39]

Morphological analysis from SEM micrographs also agrees with rheological measurements. At lower concentrations, the well-distributed MWCNTs-rich regions enhance the viscosity and

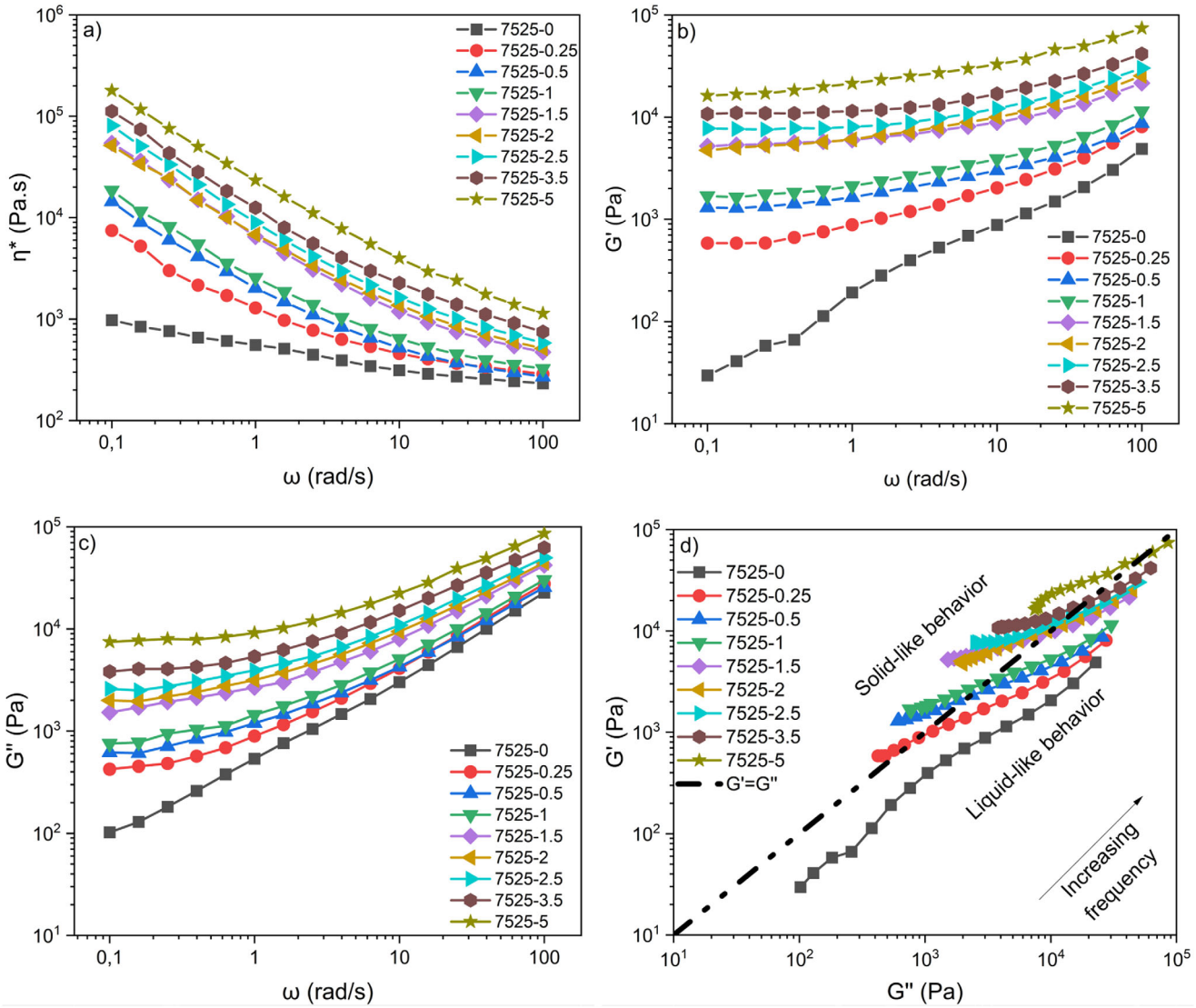

Figure 4. Viscoelastic properties of the PA6/PA12 75/25 blend and the nanocomposites with different contents of MWCNTs. a) η^* versus ω, b) G' versus ω, c) G'' versus ω and d) G' versus G''.

both moduli, indicating improved reinforcements of the polymer matrix. However, as the MWCNTs-rich regions become larger and denser at higher loadings, the rheological properties like storage and loss modulus increase due to the formation of a network structure, affecting the material's flow behavior.

Figure 4d illustrates the relationship between G' and G'' and can be utilized to examine and discern differences in the microstructure of the neat blend and nanocomposites. The neat blend exhibited a liquid-like behavior, where G′ < G″. Conversely, with minimal incorporation of MWCNT, there was a transition from liquid-like behavior to solid-like behavior at lower frequencies, indicating that the percolation threshold had been surpassed. Moreover, as the content of MWCNT increased further, this crossover point occurred at higher frequencies, resulting in a material that displayed more solid-like behavior rather than liquid-like behavior.[39,40]

The rheological percolation threshold is an important point in the behavior of filled polymers. This means that a continuous network has formed among the fillers within the polymer matrix, resulting in a transition from liquid-like to solid-like behavior.[26,41] The percolation threshold was determined following a power law equation (Equation (3)),

$$G' = G_0\left(\rho - \rho_{c,G'}\right)^{t_{G'}} \quad (3)$$

where G' is the storage modulus (at 0.1 rad/s), G_0 is the characteristic storage modulus of the blend, ρ is the volume fraction of filler, $\rho_{c,G'}$ is the volume fraction at the percolation threshold and $t_{G'}$ is the critical exponent. **Figure 5** shows the fitting performed with Equation (3) (Adj. $R^2 = 0.90$) with a rheological percolation threshold $\rho_{c,G'} = 2.48$ *vol.*% $= 0.16$ *wt.*%, a characteristic storage modulus $G_0 = 2.51$ and the critical exponent $t_{G'} = 0.95$.

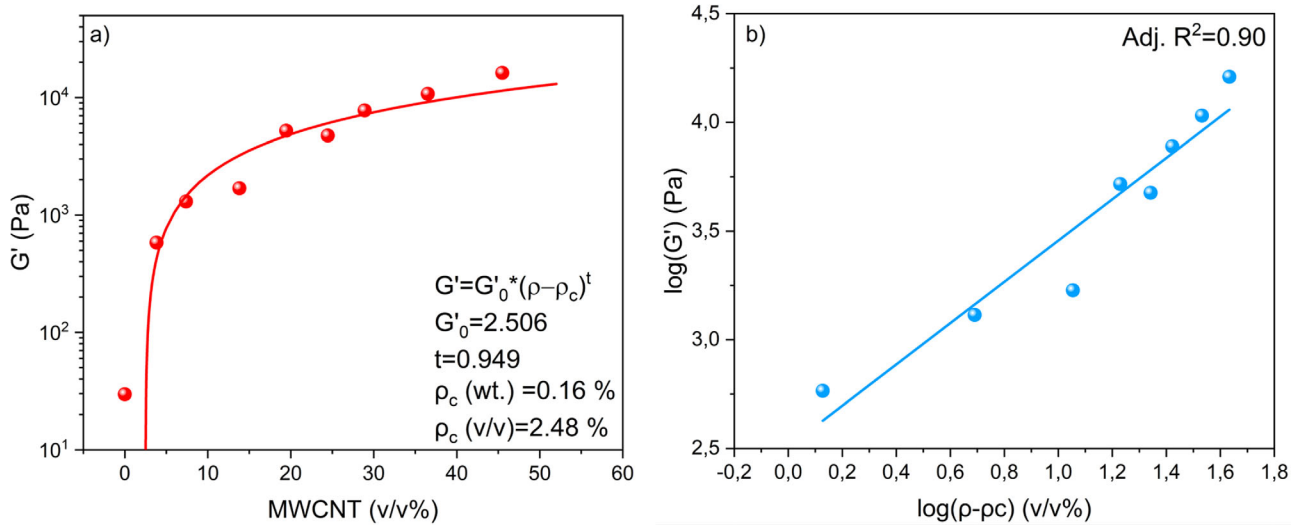

Figure 5. a) Rheological percolation threshold of the PA6/PA12 75/25 blend and the nanocomposites with different contents of MWCNT and b) log-log plot of G' versus $(\rho - \rho_{c,G'})$.

3.4. Electrical Properties

The electrical percolation threshold plays a crucial role in composite materials, reflecting the shift from being an insulator to becoming conductive. This transition is observed when there is a formation of continuous paths that allow the flow of electrons within the non-conductive polymeric matrix. When reaching the electrical percolation threshold, there is a sudden increase in electrical conductivity, indicating the successful establishment of these interconnected pathways.[42] It can be calculated following the power law Equation (4), similar to the rheological percolation threshold.

$$\sigma = \sigma_0 \left(\rho - \rho_{c,\sigma}\right)^{t_\sigma} \tag{4}$$

where σ is the volumetric conductivity, σ_0 is the characteristic volume conductivity of the blend, ρ is the volume fraction of filler, $\rho_{c,\sigma}$ is the volume fraction at the percolation threshold and t_σ is the critical exponent. The critical exponent t could be related to the connectivity and aspect ratio of the fillers, as well as to the interparticle electrical conduction mechanisms.[43]

The effect of the filler content on the electrical conductivity of the nanocomposites was investigated in this work. The results plotted in **Figure 6** shows the best linear fit (Adj. $R^2 = 0.96$) was found for $\rho_{c,\sigma} = 36.55$ *vol.%* $= 3.50$ *wt.%*, a characteristic electrical conductivity $\sigma_0 = 10.10$ S/cm and a critical exponent $t_\sigma = 6.33$. At low filler contents, the electrical conductivity is dominated by the insulating polymer matrix. However, as the filler content increases, the filler particles begin to form a percolating

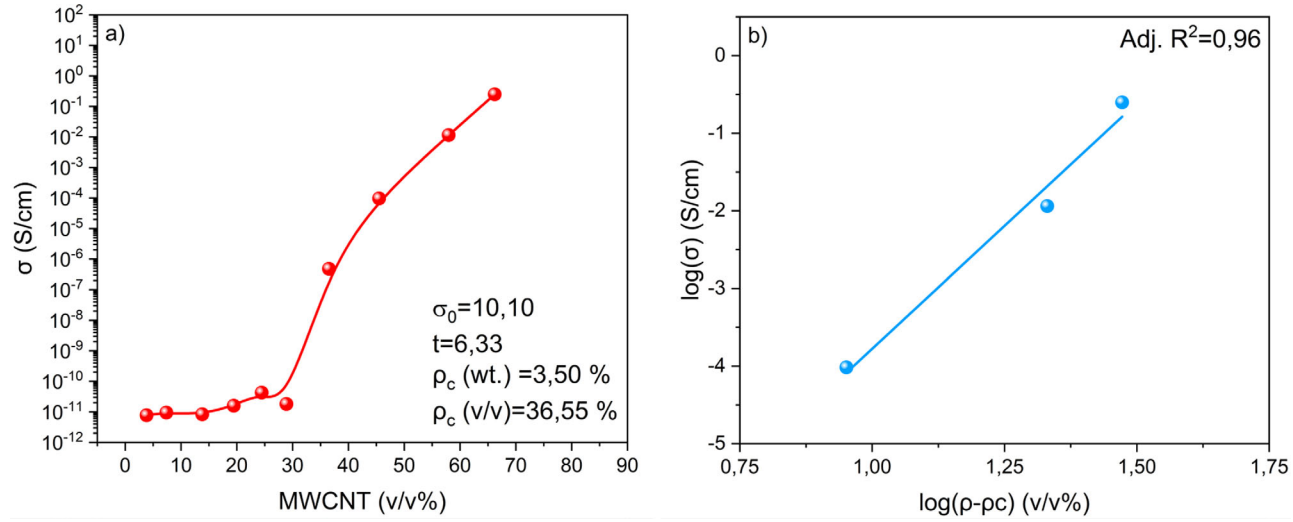

Figure 6. Electrical percolation threshold of the PA6/PA12 75/25 blend and the nanocomposites with different contents of MWCNTs and b) log-log plot of σ versus $(\rho - \rho_{c,\sigma})$.

network in agreement with the formation of a dense interconnected network evidenced in the morphology analysis, which allows electricity to flow through the material.

A high *t*-value as such obtained in this work, reflects a gradual increase of σ with filler content and significantly exceeds classical percolation theory predictions of 1.6–2.0 for three-dimensional systems.[35,44] Such deviation from universal behavior has been extensively documented in polymer composites suggesting that tunneling is the dominant conduction mechanism between filler particles.[45,46] Ezquerra et al.[47] observed a high *t* value ($t \approx 6.27$) in graphite composites which they related to the existence of tunneling conduction in their composites. Similar behavior was also observed in graphene composites by Tan et al.[48] ($t = 6.92$) supporting the Balberg's theoretical framework which explains high *t* values ($t > 4$) through tunneling distance distributions.[49] More related to this work, for polyamide 6/MWCNT systems, Kazemi et al.[35] reported $t = 6.22$ attributing to tunneling as the dominant mechanism of electron conduction between MWCNTs.

While for filler contents lower than 3.5 wt.% of filler (electrical threshold) the sea-island morphology was barely changed, for MWCNTs contents around this value interconnected networks of MWCNT-rich regions started to form. Further increasing filler loading led to more dense networks. In comparison, Arboleda et al.[14] reported a significantly lower electrical percolation threshold of 0.42 wt.% MWCNTs in PA12/PA6 50/50 nanocomposites using a PA12 masterbatch. This remarkably low threshold was ascribed to the preferential localization of MWCNTs at the polyamides interface and the preservation of the nanotubes' high aspect ratio during processing. The difference in electrical percolation thresholds between the two studies could be attributed to the use of different masterbatches and processing conditions, which would have influenced the dispersion and distribution of MWCNTs within the polymer blend.

4. Conclusion

Nanocomposites based on an immiscible blend of PA6 and PA12 (75/25) and different contents of MWCNTs were successfully obtained. The materials were characterized in terms of morphology, and thermal, rheological and electrical behavior.

The incorporation of MWCNTs into the PA6/PA12 blend matrix induced a transition from a sea-island structure to a more interconnected MWCNTs-rich zones network. These morphological changes were closely correlated with the thermal and electrical behavior of the nanocomposites. Notably, more pronounced changes occurred beyond the electrical percolation threshold (3.5 wt.% MWCNT). This was attributed to the formation of interconnected networks of MWCNT-rich zones which enhanced the electrical conductivity of the material (from 7.7×10^{-12} S.cm^{-1} to 0.25 S.cm^{-1}).

Regarding the thermal properties, the MWCNTs acted as nucleating agents mainly in the polyamide 6 increasing its melting temperature and the heterogeneity of its crystals population.

With the increment of the MWCNTs content, rheological percolation (at 0.16 wt.%) occurs prior to electrical percolation, indicating the formation of a continuous network among the fillers within the polymer matrix not sufficiently interconnected to generate an electrically conductive network.

Ultimately, the observed increase in electrical conductivity beyond the percolation threshold (at 3.5 wt.%) highlights the significance of establishing a well-dispersed and interconnected network of MWCNTs within the polymer matrix.

In summary, the relationship among the different properties investigated herein emphasizes the potential for optimizing material performance by carefully controlling MWCNT content and processing strategies, which determine the filler dispersion and distribution within the polymer matrix.

This study provides important insights for advancing the design and development of novel conductive polymer nanocomposites, which seem to be highly applicable for various technologies that demand electrical properties, including electromagnetic interference (EMI) shielding and advanced sensing applications.

Supporting Information

Supporting Information is available from the Wiley Online Library or from the author.

Acknowledgements

This research was financially supported by the ANPCyT (PICT 2018 4217), the University of Buenos Aires (UBACyT 2023 20020220100207BA) and Xunta de Galicia-FEDER (Program of Consolidation and structuring competitive research units (ED431C 2023/24). The authors also gratefully acknowledge the National Research Council of Argentina (CONICET) for Tomas Arnal's scholarship. Open access funding was provided by the Universidade da Coruna/CISUG.

Conflict of Interest

The authors declare no conflict of interest.

Data Availability Statement

Research data are not shared.

Keywords

conductive polymer composites, multi-walled carbon nanotubes, nanocomposites, polyamide blends

Received: November 28, 2024
Revised: February 21, 2025
Published online:

[1] S. Sankaran, K. Deshmukh, M. B. Ahamed, S. K. Khadheer Pasha, *Appl. Sci. Manuf.* **2018**, *114*, 71.
[2] N. Maruthi, M. Faisal, N. Raghavendra, *Synth. Metals* **2021**.
[3] S. Zheng, Y. Wang, Y. Zhu, C. Zheng, *Polym. Compos.* **2024**, *45*, 43.
[4] J. Li, E. Masghouni, M. Granger, G. Sudre, P. Alcouffe, D. Muller, V. S. Nguyen, B. Bayard, A. Serghei, B. Sauviac, A. Maazouz, K. Lamnawar, *Macromol. Mater. Eng.* **2024**, *309*, 2300344.
[5] H. Liu, Q. Li, S. Zhang, R. Yin, X. Liu, Y. He, K. Dai, C. Shan, J. Guo, C. Liu, C. Shen, X. Wang, N. Wang, Z. Wang, R. Wei, Z. Guo, *J. Mater. Chem. C* **2018**, *6*, 12121.

[6] J. Chen, Y. Zhu, J. Huang, J. Zhang, D. Pan, J. Zhou, J. E. Ryu, A. Umar, Z. Guo, *Polym. Rev.* **2020**, *61*, 157.
[7] L. Wang, H. Wang, Q. Wan, J. Gao, *J. Polym. Sci.* **2023**, *61*, 3167.
[8] S. Mishra, L. Unnikrishnan, S. K. Nayak, S. Mohanty, *Macromol. Mater. Eng.* **2019**, *304*, 1800463.
[9] S. Lage-Rivera, A. Ares-Pernas, M. Abad, *Int. J. Energy Res.* **2022**, *46*, 10475.
[10] M. G. Tadesse, A. S. Ahmmed, J. F. Lübben, *J. Compos. Sci.* **2024**, *8*, 53.
[11] Y. Huang, S. Kormakov, X. He, X. Gao, X. Zheng, Y. Liu, J. Sun, D. Wu, *Polymers* **2019**, *11*, 187.
[12] H. Pang, L. Xu, D.-X. Yan, Z.-M. Li, *Prog. Polym. Sci.* **2014**, *39*, 1908.
[13] L. Arboleda, A. Ares, M. J. Abad, A. Ferreira, P. Costa, S. Lanceros-Mendez, *J. Polym. Res.* **2013**, *20*, 326.
[14] L. Arboleda-Clemente, A. Ares-Pernas, X. García, S. Dopico, M. J. Abad, *Polym. Compos.* **2017**, *38*, 2679.
[15] B. Krause, L. Kroschwald, P. Pötschke, *Polymers* **2019**, *11*, 122.
[16] T. Arnal, P. Eisenberg, M. J. Abad, A. Ares-Pernas, C. R. Bernal, *Polym. Eng. Sci.* **2024**, *64*, 1246.
[17] Z. Starý, H. Münstedt, presented at *AIP Conference Proceedings*, American Institute of Physics Inc, New York **2017**, 1843.
[18] J. Banerjee, K. Dutta, in *Polymer Composites*, John Wiley and Sons Inc, Hoboken, New Jersey **2019**, pp. 4473.
[19] M. R. Watt, R. A. Gerhardt, *J. Compos. Sci.* **2020**.
[20] R. Salehiyan, S. S. Ray, *Macromol. Mater. Eng.* **2019**, *304*, 1800431.
[21] H. E. Bair, P. K. Gallagher, M. Jaffe, D. Raucher, in *Thermal Characterization of Polymeric Materials*, Elsevier, Amsterdam, Netherlands **1981**.
[22] S. Gogolewski, K. Czerntawska, M. Gastorek, *Colloid Polym. Sci.* **1980**, *258*, 1130.
[23] K. T. Company, in *Low Level Measurements Handbook*, 7th Ed. Tektronix INC, Beaverton **2016**
[24] N. Chuaponpat, T. Ueda, A. Ishigami, T. Kurose, H. M. Ito, *Polymers* **2020**, *12*, 1083.
[25] P. Pötschke, D. R. Paul, *J. Macromol. Sci. – Polym. Rev.* **2003**, *43*, 87.
[26] X. Qi, J. Yang, N. Zhang, T. Huang, Z. Zhou, I. Kühnert, P. Pötschke, Y. Wang, *Prog. Polym. Sci.* **2021**, *123*, 101471.
[27] L. Arboleda-Clemente, A. Ares-Pernas, X. X. García-Fonte, M. J. Abad, *J. Mater. Sci.* **2016**, *51*, 8674.
[28] I. O. Navas, M. Arjmand, U. Sundararaj, *RSC Adv.* **2017**, *7*, 54222.
[29] Z. Liu, W. Peng, Y. Zare, D. Hui, K. Y. Rhee, *RSC Adv.* **2018**, *8*, 19001.
[30] J. Yang, X. Qi, N. Zhang, T. Huang, Y. Wang, *Compos. Commun.* **2018**, *7*, 51.
[31] R. Socher, B. Krause, S. Hermasch, R. Wursche, P. Pötschke, *Compos. Sci. Technol.* **2011**, *71*, 1053.
[32] S. Kumar, M. R. Ramesh, M. Doddamani, S. M. Rangappa, S. Siengchin, *Polym. Test.* **2022**, *114*, 107703.
[33] S. Zhou, A. N. Hrymak, M. R. E. Kamal, *Compos. Part A Appl. Sci. Manuf.* **2017**, *103*, 84.
[34] X. T. Chen, H. J. Liu, X. Y. Zheng, in *Crystallization and Mechanical Properties of Multi-Walled Carbon Nanotubes Modified Polyamide 6*, (Ed: P. Chen), CRC Press, Boca Raton **2015**.
[35] Y. Kazemi, A. R. Kakroodi, L. H. Mark, T. Filleter, C. B. Park, *Polymer* **2019**, *178*, 121684.
[36] A. Abbasi Moud, A. Javadi, H. Nazockdast, A. Fathi, V. Altstaedt, *J. Polym. Sci. Part B Polym. Phys.* **2015**, *53*, 368.
[37] S. K. Sahu, N. D. Badgayan, P. S. R. Sreekanth, *Biointerface Res. Appl. Chem.* **2022**, *12*, 5709.
[38] C. Zhang, X. Liu, H. Liu, Y. Wang, Z. Guo, C. Liu, *Polym. Test.* **2019**, *75*, 367.
[39] A. Bata, D. Nagy, Z. Weltsch, *Polymers* **2022**, *14*, 5257.
[40] B. N. Duc, Y. Son, *J. Compos. Mater.* **2022**, *56*, 3529.
[41] R. Arrigo, G. Malucelli, *Materials* **2020**, *13*, 1.
[42] A. V. Eletskii, A. A. Knizhnik, B. V. Potapkin, J. M. Kenny, *Physics-Uspekhi* **2015**, *58*, 209.
[43] I. Y. Forero-Sandoval, A. P. Franco-Bacca, F. Cervantes-Álvarez, C. L. Gómez-Heredia, J. A. Ramírez-Rincón, J. Ordonez-Miranda, J. J. Alvarado-Gil, *J. Appl. Phys.* **2022**, *131*, 230901.
[44] K. Dai, X. Xu, Z. Li, *Polymer* **2007**, *48*, 849.
[45] Z. Rubin, S. A. Sunshine, M. B. Heaney, I. Bloom, I. Balberg, *Phys. Rev. B* **1999**, *59*, 12196.
[46] L. Karásek, B. Meissner, S. Asai, M. Sumita, *Polym. J.* **1996**, *28*, 121.
[47] T. A. Ezquerra, M. Kulescza, C. S. Cruz, F. J. Baltá-Calleja, *Adv. Mater.* **1990**, *2*, 597.
[48] Y. Tan, L. Fang, J. Xiao, Y. Song, Q. Zheng, *Polym. Chem.* **2013**, *4*, 2939.
[49] I. Balberg, *J. Appl. Phys.* **2020**, *128*, 204304.

